PNAS
www.pnas.org

Supplementary Information for

Bubble pinch-off in turbulence

Daniel J. Ruth, Wouter Mostert, Stéphane Perrard, and Luc Deike

Luc Deike.
E-mail: ldeike@princeton.edu

This PDF file includes:

Figs. S1 to S19
References for SI reference citations

Supplementary Video 1 Movie corresponding to figure 2 in the main paper. Top left: Close-up views from the two high speed cameras. Top right: Neck diameters d_x and d_y in the two views during the pinch-off exhibit oscillations, while the averaged diameter follows the classic self-similar scaling. Bottom left: Velocity of the four measured thinning points. Bottom right: Difference $\Delta r = (d_x - d_y)/2$ as a function of mean neck diameter.

Supplementary Video 2 Movie corresponding to figure 3 A-B in the main paper. Top left: Close-up views from the two high speed cameras. A kink like structure becomes visible towards the end of the pinch-off. Top right: Neck diameters d_x and d_y in the two views during the pinch-off, together with the averaged diameter. Bottom left: Velocity of the four measured thinning points. Bottom right: Difference $\Delta r = (d_x - d_y)/2$ as a function of mean neck diameter.

Supplementary Video 3 Movie of one turbulent pinch-off with a persistent asymmetry in the neck shape until a kink structure forms. Top left: Close-up views from the two high speed cameras. Top right: Neck diameters d_x and d_y in the two views during the pinch-off, together with the averaged diameter. Bottom left: Velocity of the four measured thinning points. Bottom right: Difference $\Delta r = (d_x - d_y)/2$ as a function of mean neck diameter.

1. Experimental methods

We provide here more details on the experimental setup, data acquisition and processing.

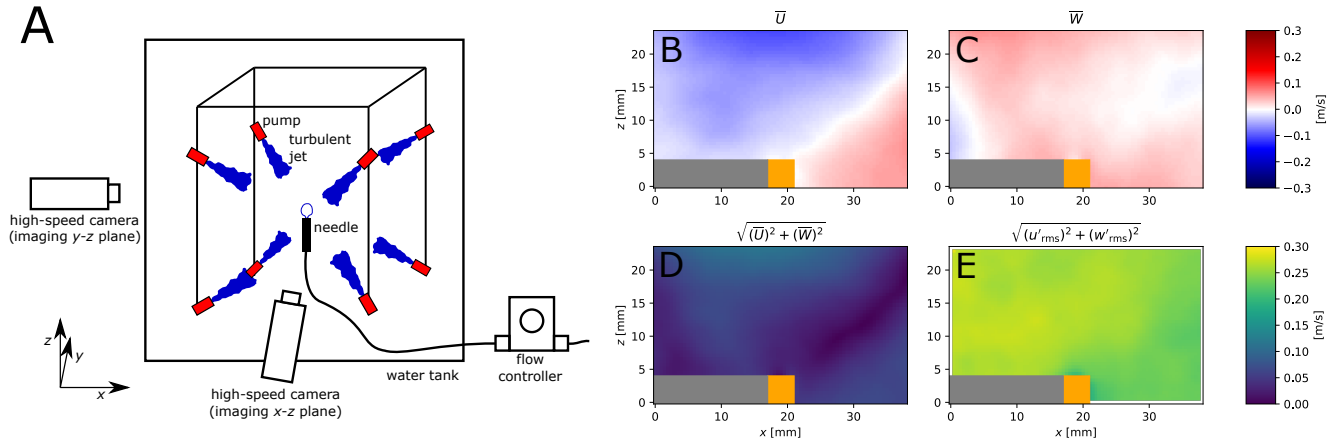

Fig. S1. (a) Sketch of the experimental setup. The turbulence tank consists of eight submerged pumps. (b) and (c) The horizontal and vertical components of the mean flow, respectively, obtained by particle image velocimetry in the $\epsilon = 1500\,\mathrm{cm}^2/\mathrm{s}^3$ case. The needle is colored orange and the portion of the image in which the laser sheet is blocked by the needle is colored grey. (d) and (e) The speed of the mean flow and the intensity of the fluctuations.

A. Experimental setup. The experiment is sketched in Figure S1 (a). Turbulence in the water is created by eight submerged pumps whose outlets are attached via flexible tubing to nozzles arranged at the vertices of a $\sim 28\,\mathrm{cm}$ cube and pointed towards the cube's center (for the sake of simplicity these tubes are omitted from Figure S1) (a). Inspired by the work of Variano and Cowen (1) and Hwang and Eaton (2), this setup induces a largely homogeneous, isotropic flow in the cube center. A needle with inner diameter between 1.4 mm and 4.8 mm is fixed within the turbulence region and connected to an Alicat flow rate controller through which air is fed. The needle is typically positioned such that the mean vertical flow around its tip is slightly positive, which makes the neck region visible to the cameras in a large portion of the pinch-off events. Varying the needle size and turbulence dissipation rate, we record ~ 300 cases of a bubble pinching-off in turbulence and ~ 40 cases of pinch-off in a quiescent flow. We discard cases in which the neck region is not well-resolved in the view of either of the two cameras used, as well as ~ 10 cases in which a thin air filament persists, and sometimes grows in width just before pinch-off, for far longer than is typical.

B. Turbulence measurements. Particle image velocimetry (PIV) with a single camera is used to resolve the horizontal and vertical components of the flow u and w in a $3.8\,\mathrm{cm} \times 2.3\,\mathrm{cm}$ region around the needle. For each ϵ level, ten high-speed movies 0.8 s in duration, separated by 10 s, were obtained with a pixel size of 30 µm. The flowfield was resolved using PIVLab (3). First, the horizontal and vertical components of the mean flow $\overline{U}$ and $\overline{V}$ are obtained by averaging all realizations of the instantaneous flowfield, and are shown in Figure S1 (b) and (c) for the $\epsilon = 1500\,\mathrm{cm}^2/\mathrm{s}^3$ case. The needle is placed in a region of slightly-upwards mean flow, which increases the portion of pinch-off events in which the neck region is visible. Results from the lower and higher ϵ values look qualitatively similar but differ in magnitude.

The mean flow speed $\sqrt{(\overline{U})^2 + (\overline{W})^2}$ is shown in Figure S1 (d) for the $\epsilon = 1500\,\mathrm{cm}^2/\mathrm{s}^3$ case. The intensity of the turbulence is characterized by the r.m.s. velocity fluctuations $\sqrt{\overline{u'^2} + \overline{w'^2}}$, with $u' = u - \overline{U}$ and $w' = w - \overline{W}$, which is shown in Figure S1 (c). The typical fluctuations are multiple times greater than the mean speed of the flow.

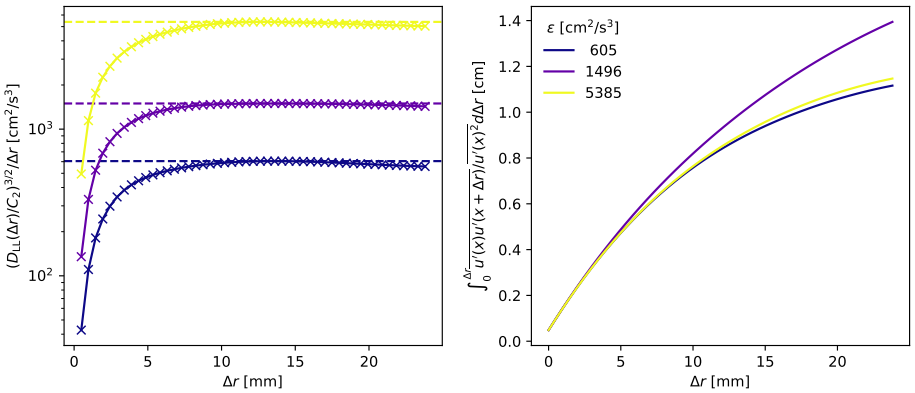

Fig. S2. *Left*, the compensated longitudinal structure function, $(D_{\mathrm{LL}}(r)/C_2)^{3/2}/r$, (markers) and the determined dissipation rates ϵ (dashed lines). *Right*, the integral of the spatial autocorrelation used to determine the integral length scale L_{int}.

The dissipation rate is calculated with the x-direction longitudinal structure function $D_{\mathrm{LL}}(\Delta r) = \overline{(u'(x,z,t) - u'(x+\Delta r,z,t))^2}$, averaged over x (once going from left-to-right in the image above, once going right-to-left), z (above the top of the needle), and t, in only the x-direction to calculate the dissipation rate. D_{LL} is then compensated as $(D_{\mathrm{LL}}(r)/C_2)^{3/2}/r$, with $C_2 = 2.0$ the Kolmogorov constant (4). The resulting curves and their maximum values are shown in Figure S2 (a). The three values of ϵ used in this study are approximately $600\,\mathrm{cm}^2/\mathrm{s}^3$, $1500\,\mathrm{cm}^2/\mathrm{s}^3$, and $5400\,\mathrm{cm}^2/\mathrm{s}^3$.

Finally, the integral length scale is estimated by integrating the spatial autocorrelation function for the velocity fluctuations, $L_{\mathrm{int}} = \int_{\Delta r=0}^{\infty} \overline{u'(x,z,t)u'(x+\Delta r,z,t)}/\overline{u'(x,z,t)^2} d\Delta r$. The resulting curves are shown in Figure S2. While the resolved field is not large enough to extract the asymptotic value of the integral, we can visually estimate that it is approximately $L_{\mathrm{int}} = 1.3\,\mathrm{cm}$ and not a strong function of ϵ.

With ϵ calculated, the Kolmogorov microscale is defined as $\eta = (\nu^3/\epsilon)^{1/4}$, where ν is the kinematic viscosity of water. For the three increasing values of ϵ, the Kolmogorov microscale is 58 µm, 47 µm, and 34 µm. Similarly, the Taylor microscale is estimated as $\lambda = (15\overline{(u')^2}\nu/\epsilon)^{1/2}$, and for the three increasing values of ϵ is 1.7 mm, 1.7 mm, and 1.2 mm. This is comparable to the initial size of the neck as pinch-off begins, suggesting that the bubble is initially within the inertial subrange of the turbulence.

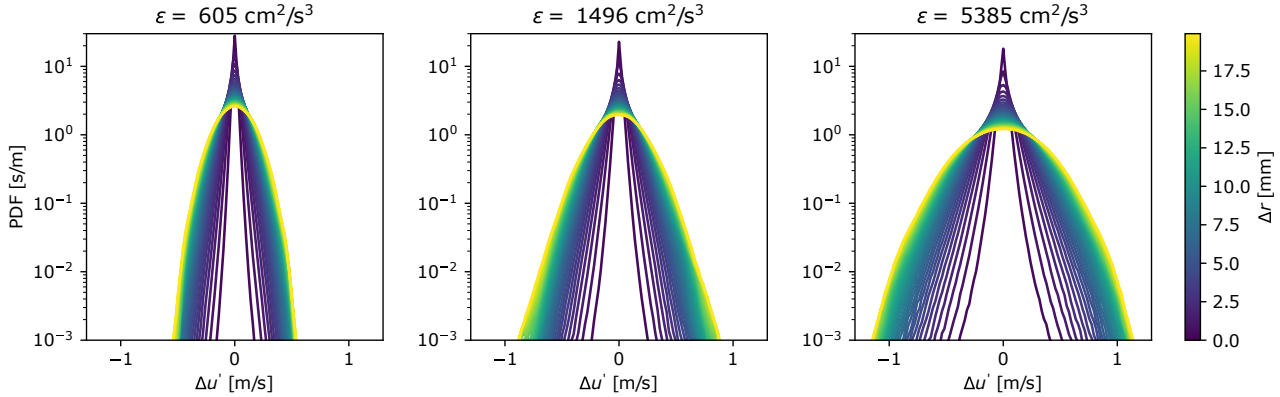

Fig. S3. Distributions of the velocity difference, $\Delta u' = \langle u'(x+\Delta r) - u'(x)\rangle$, over a range of spatial separations, Δr (color-coded) going from $0.5\,\mathrm{mm}$ to $2.0\,\mathrm{cm}$, for each value of ϵ. Velocity fluctuations at the size of the neck never reach the magnitude of the neck collapse velocity, even in the tail of the distribution.

Figure S3 shows the distributions of velocity fluctuation $\Delta u' = \langle u'(x+\Delta r) - u'(x)\rangle$ difference calculated over various spatial separations Δr, for a range of spatial locations and for the whole time series. Even in the tails of the distributions, the turbulent velocity difference never reaches the large velocities associated with the appearance of the kink in the interface, which rules out the direct action of a turbulent eddy in the kink formation process.

C. Imaging. The back-lit imaging of the pinch-off is done with two cameras, similar to (5, 6), which provide a measure of the neck's asymmetry with views from two orthogonal angles. One camera (Phantom v2012) films at $1/\Delta t = 100\,000$ fps and a pixel size $\Delta x = 22$ µm, while the other (Phantom VEO 440-L) films at $1/\Delta t = 24000$ to $29\,000$ fps and $\Delta x = 29$ µm. Due to hardware limitations, the VEO 440-L only resolves 48 to 64 pixels in the vertical direction, while the other camera resolves 320 pixels vertically. The pinch-off time is identified independently from each recording as the first frame in which the neck is

visibly separated.

D. Image processing and mapping to 3-D space. Movies of pinch-off are obtained in the laboratory-referenced $x-z$ and $y-z$ planes. Two simultaneous images are shown in Figure S4 (a-b). As a first step in mapping 2-D imaged points to 3-D locations, we identify the orientation of the bubble neck in each view, $\theta_x(t)$ and $\theta_y(t)$. θ_i is the angle of the bubble axis (measured from the z axis to the i axis), determined by considering the line normal to the shortest line segment drawn across opposing sides of the neck. $\theta_x(t)$ and $\theta_y(t)$ are then interpolated onto common t values and the orientation of the neck axis z' relative to the laboratory axes is calculated as

$$\tan\theta(t) = \sqrt{\tan^2\theta_x(t) + \tan^2\theta_y(t)}, \quad [1]$$

$$\tan\phi(t) = \tan\theta_x(t)/\tan\theta_y(t), \quad [2]$$

where θ is the angle from z to z' and ϕ is the angle of the projection of z' onto the $x-y$ plane measured from the x axis. To account for an angular drift of the bubble in time due to the frozen turbulent flow while removing artifacts which complicate the angle detection close to pinch-off, we replace $\theta(t)$ and $\phi(t)$ with linear fits to their instantaneous data taken within $\sim 2\,\text{ms} \leq (t_0 - t) \leq \sim 8\,\text{ms}$, with these limits adjusted on a case-by-case basis. This assumes that the mean flow around the bubble is a rotational flow pivoting about the pinch-off point, and the pinch-off plane in which the neck sizes are tracked pivots accordingly. In some cases when the automated detection fails, the orientation of the bubble is imposed manually. The quality of the fit is verified visually by ensuring that the assumed neck axis is aligned with the bubble neck. θ_x and θ_y are the angles from the vertical axis to the red lines in Figure S4 (a-b).

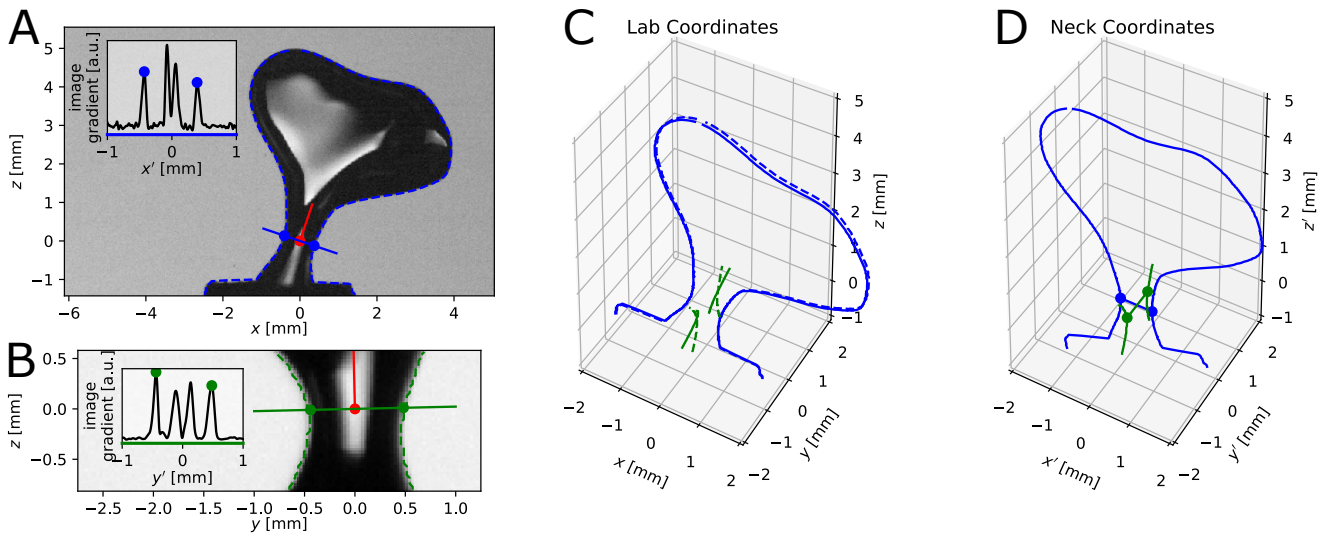

Fig. S4. Illustration of the neck detection and 3-D mapping method. (a-b) The images obtained from the two cameras. The pinch-off point is shown as the red dot. The projection of the neck axis z' on the resolved planes is shown as the red line, and the projections of the x' and y' axes are shown as the solid blue and green lines, respectively. The insets show the gradient of the image along these two axes, and the dots correspond to the detected location of the two sides of the neck. The contours of the bubble are shown in the laboratory coordinate system (x, y, z) in (c) and in the bubble neck coordinate system (x', y', z') in (d). The dashed lines in (c) show the naive position of the bubble contours before their depth is inferred.

The pinch-off locations in laboratory coordinates in the planar views, $(c_{x,0}, c_{z,0})$ and $(c_{y,0}, c_{z,0})$ are determined manually, which enforces that $z = 0$ corresponds to the same physical plane in each view. The pinch-off point $(c_{x,0}, c_{y,0}, c_{z,0})$ is taken as the origin of both the laboratory and neck coordinate systems. The red dots in Figure S4 (a-b) show the pinch-off location in the two planes.

To determine $d_x(t)$, the resolved neck diameter viewed from the $x-z$ plane, we first use the bubble neck orientation $(\theta(t), \phi(t))$ to infer the depth c_y in the y-direction of any point (c_x, c_z) imaged on the bubble interface. As a best guess, we choose c_y which brings the point as close as possible to the bubble axis, z'. Given the depth of the point c_y and a point at a position z' along the neck axis, the squared distance between the two points is

$$F = (\Delta x)^2 + (\Delta y)^2 + (\Delta z)^2 \quad [3]$$

$$= \left(c_x - z'\sin\theta\cos\phi\right)^2 + \left(c_y - z'\sin\theta\sin\phi\right)^2 + \left(c_z - z'\cos\theta\right)^2. \quad [4]$$

To find the minimum value of F we take the two partial derivatives,

$$\frac{\partial F}{\partial z'} = -2\left(c_x - z'\sin\theta\cos\phi\right)\sin\theta\cos\phi - 2\left(c_y - z'\sin\theta\sin\phi\right)\sin\theta\sin\phi - 2\left(c_z - z'\cos\theta\right)\cos\theta, \quad [5]$$

$$\frac{\partial F}{\partial c_y} = 2\left(c_y - z'\sin\theta\sin\phi\right). \quad [6]$$

Setting both partial derivatives to 0 and solving the system of equations gives

$$z' = \frac{c_1 \sin\theta\cos\phi + c_z\cos\theta}{\sin^2\theta\cos^2\phi + \cos^2\theta}, \quad [7]$$

$$c_y = \frac{\sin\theta\sin\phi}{\sin^2\theta\cos^2\phi + \cos^2\theta}\left(c_1\sin\theta\cos\phi + c_z\cos\theta\right). \quad [8]$$

Similarly if we locate a point in the $y-z$ plane and want to infer its position in the x direction, we now use the partial derivative

$$\frac{\partial F}{\partial c_x} = 2\left(c_x - z'\sin\theta\cos\phi\right) \quad [9]$$

and obtain

$$z' = \frac{c_y \sin\theta\sin\phi + c_z\cos\theta}{\sin^2\theta\sin^2\phi + \cos^2\theta}, \quad [10]$$

$$c_x = \frac{\sin\theta\cos\phi}{\sin^2\theta\sin^2\phi + \cos^2\theta}\left(c_y\sin\theta\sin\phi + c_z\cos\theta\right). \quad [11]$$

With the depth of each point in the image inferred, the 3-D locations (c_x, c_y, c_z) in laboratory coordinates are transformed into points $(c_{x'}, c_{y'}, c_{z'})$ in neck coordinates (x', y', z') by rotating each an angular distance $-\theta(t)$ about the line parallel to $\phi(t)+\pi/2$ going through the origin. The dashed blue curve in Figure S4 (c) shows the naive contour of the bubble in laboratory coordinates, in which all points obtained from the $x-z$ plane view are assumed to fall on the $y=0$ plane. The solid blue curve shows the contour with the y position inferred according to the method employed. The reconstruction in Figure S4 (d) shows the same bubble contours now in neck coordinates, where the vertical axis z' is the axis of the bubble and the x' and y' axes correspond to the solid blue and green lines shown in Figure S4 (a-b).

The contours shown in Figure S4 are used solely for determining the orientation of the bubble and for visualization. To determine d_x, the width of the bubble neck resolved in the $x-z$ plane, we use a separate image gradient-based approach. First, we compute the gradient $G(x,z)$ of the image (after applying a Gaussian blur with a standard deviation of 0.5 pixels) $I(x,z)$, which is most intense at locations where the pixels change from light to dark abruptly (such as at the bubble interface). This is defined as

$$G(x,z) = \sqrt{\left(\frac{\partial I}{\partial x}\right)^2 + \left(\frac{\partial I}{\partial z}\right)^2}. \quad [12]$$

Then, the line through G corresponding to $z'=0$, that is, the pinch-off plane's intersection with the $x-z$ plane, is extracted. This is shown as the solid blue line in Figure S4 (a-b). The location of the two opposing sides of the neck are determined by finding the outermost suitable local maxima in the gradient of the image along this line, shown in the inset in Figure S4 (a-b). With these two points determined, the neck distance is determined as $d_x = \sqrt{(c_{x',r} - c_{x',l})^2 + (c_{y',r} - c_{y',l})^2}$, (or equivalently $d_x = \sqrt{(c_{x,r} - c_{x,l})^2 + (c_{y,r} - c_{y,l})^2}$ when transformed back into laboratory coordinates), where the subscripts l and r refer to the left and right sides of the neck. The z' positions of the two points are identical and as such do not influence d_x, since our neck detection imposes that the neck falls on the $z'=0$ plane. Occasionally, the neck position is corrected manually when the automated detection fails.

A similar process is used to calculate d_y as viewed from the $y-z$ plane.

The collapse rates of the two sides of the neck imaged in the $x-z$ plane are $v_{\perp,x,l} = dc_{x',l}(t)/dt$ and $v_{\perp,x,r} = -dc_{x',r}(t)/dt$, and those of the two sides of the neck imaged in the $y-z$ plane are $v_{\perp,y,l} = dc_{y',l}(t)/dt$ and $v_{\perp,y,r} = -dc_{y',r}(t)/dt$. The reported velocity curves are smoothed by applying a rolling median filter then a rolling mean filter to the raw data, where the window

2. Additional experimental cases

A. Pinch-off without background turbulence. Figure S5 shows one example of pinch-off recorded in a quiescent background. The $\alpha = 1/2$ power-law scaling is observed.

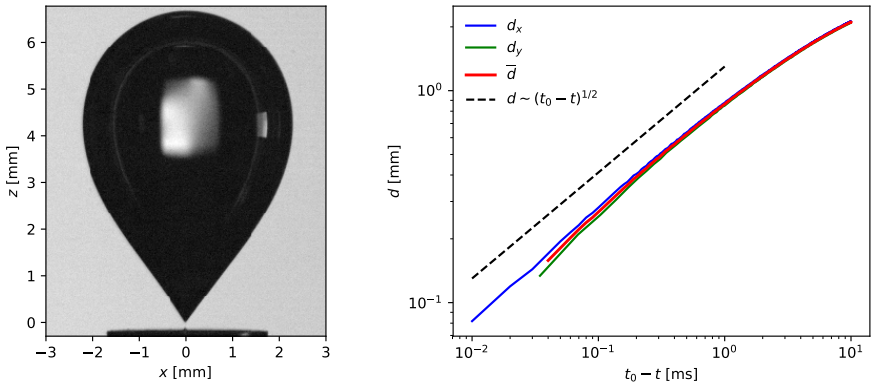

Fig. S5. Pinch-off from a needle without turbulence. *Left*, a view of the bubble in the $x - z$ plane just after pinch-off. *Right*, the tracked neck sizes and the $\alpha = 1/2$ power law.

B. Cases involving neck shape oscillations. Figure S6 presents four cases in which oscillations of the neck shape whose period can be described by the collapse model of Schmidt *et. al* (6). Fits of the model to the experimental data (the dashed lines) involve specifying an offset about which the $(d_x - d_y)/2$ signal oscillates, which was not needed for the case shown in Figure 2 in the paper.

C. Cases in which $\overline{d}$ escapes self-similarity. Figure S7 and section C give five examples of cases in which the collapse escapes self-similarity before pinch-off. The collapse velocity of the four resolved points on the bubble neck is shown in the right of each figure.

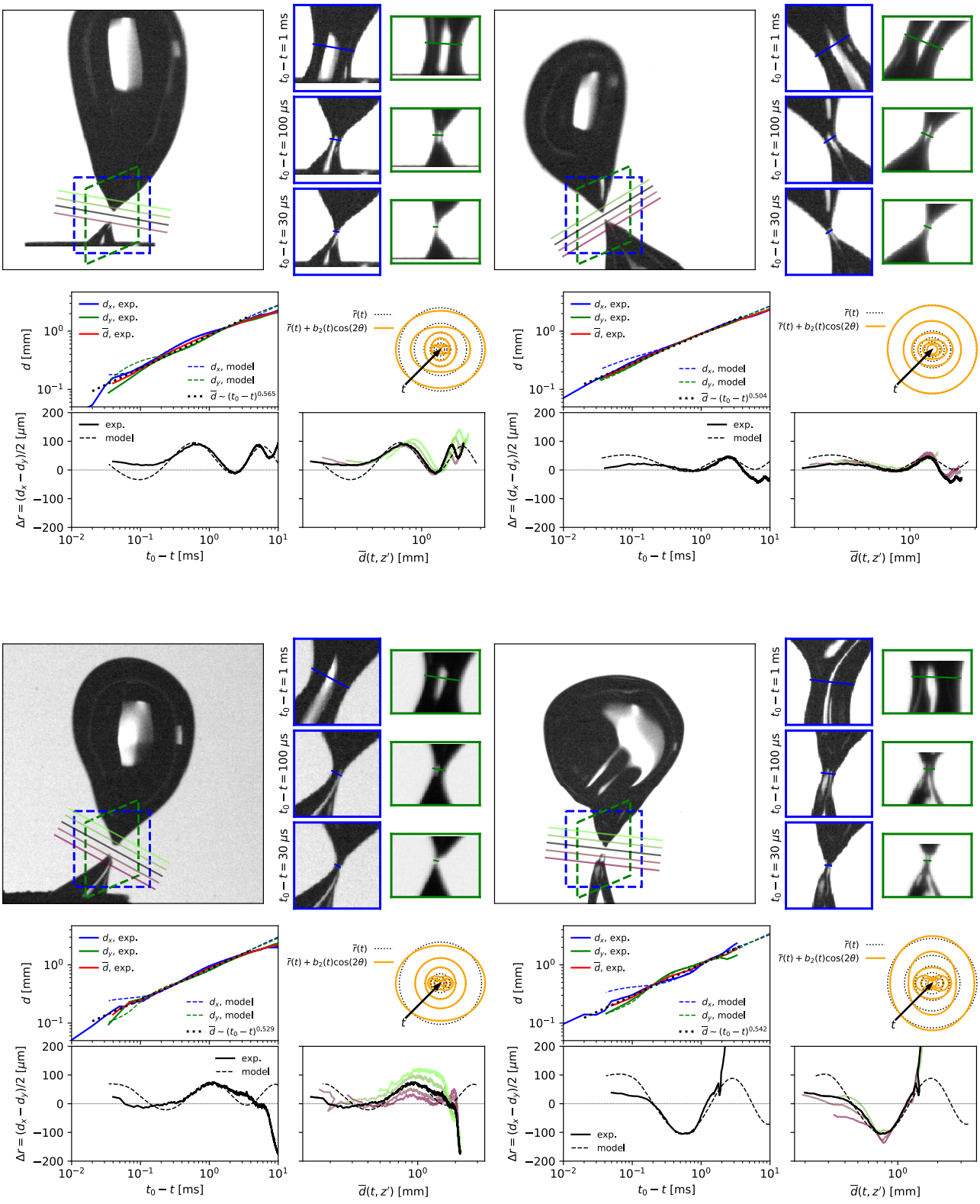

Fig. S6. Four experimental cases in which the neck cross-section oscillates in shape during the pinch-off. Refer to Figure 2 in the main paper for a description of the data presented. In some cases certain slices through the neck have been omitted when the bubble size is not completely resolved there due to the limited field of view in the $y - z$ plane. For all cases, $d_\mathrm{n} = 2.7\,\mathrm{mm}$, and clockwise from the top left, ϵ is 1500, 1500, 5400, and $1500\,\mathrm{cm}^2/\mathrm{s}^3$.

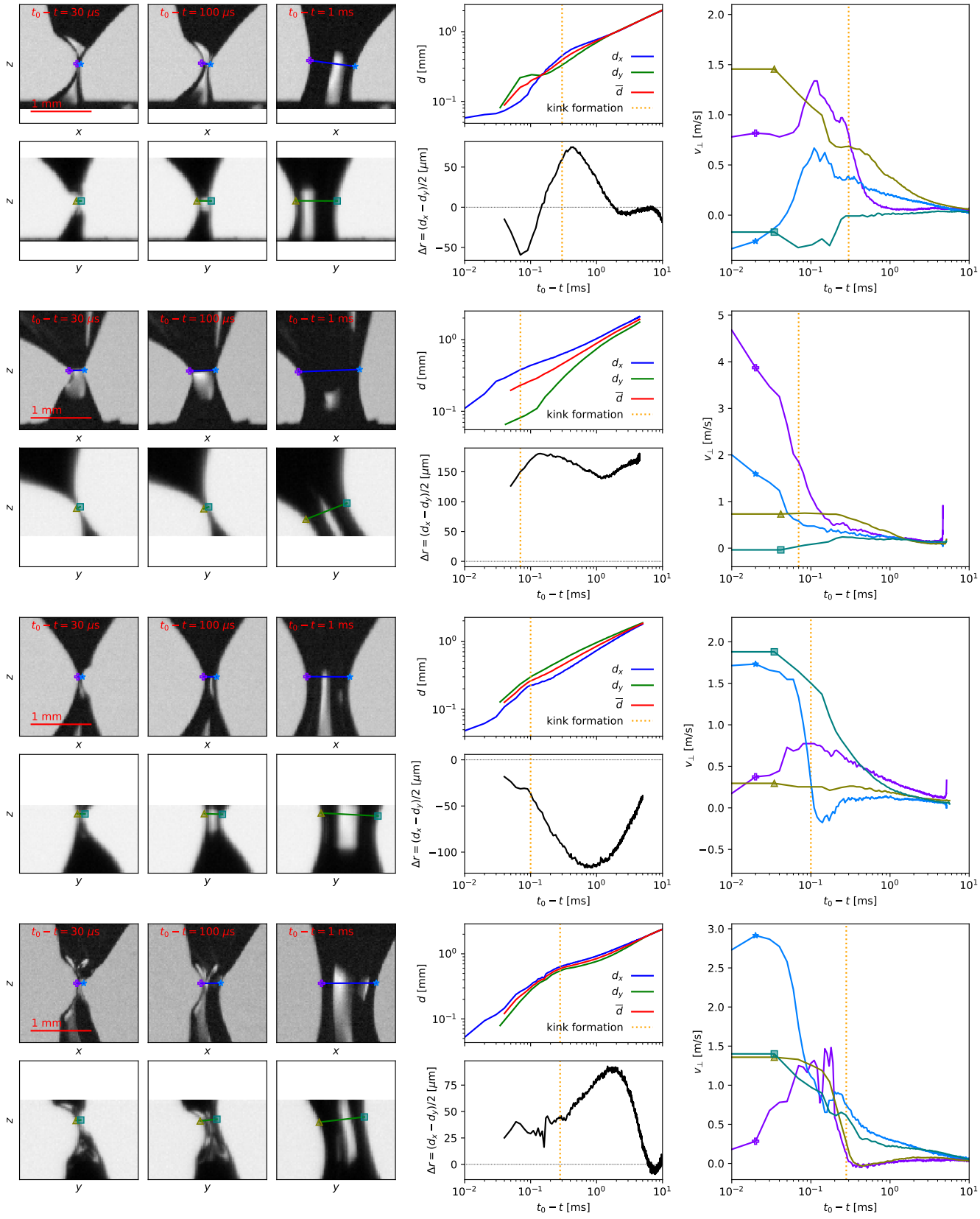

Fig. S7. Four cases in which a kink appears at the end and $\overline{d}$ escapes self-similarity, similar to those shown in Figure 3 in the paper. The kink formation time (as determined from the images) is shown as the dashed orange line; this corresponds with the jump in velocity in a side of a neck. All cases have $d_\mathrm{n} = 2.7\,\mathrm{mm}$. From top to bottom, ϵ is 600, 5400, 600, and $1500\,\mathrm{cm}^2/\mathrm{s}^3$.

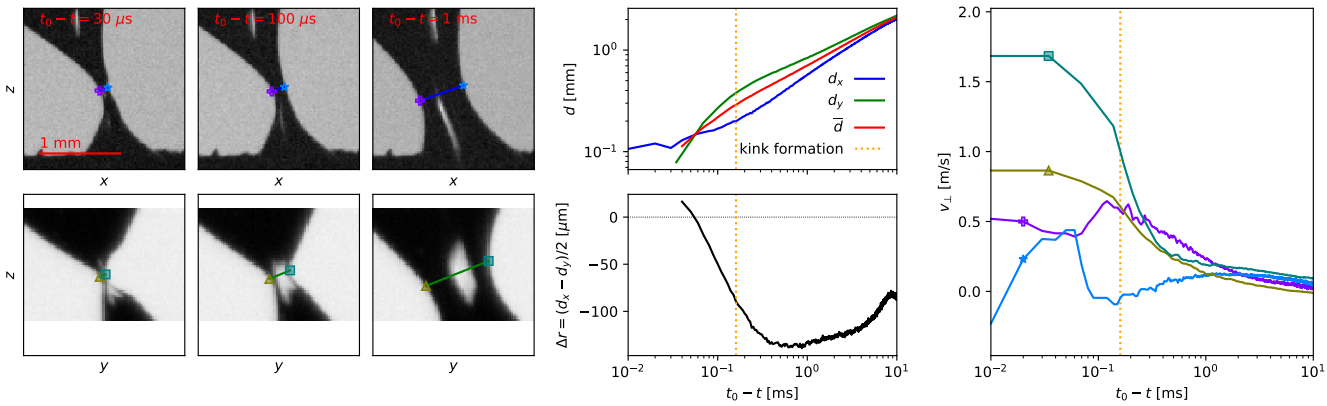

Fig. S8. See caption to Figure S7. Here, $d_\mathrm{n} = 2.7\,\mathrm{mm}$ and $\epsilon = 1500\,\mathrm{cm}^2/\mathrm{s}^3$.

D. Examples of the kink structure. The kink time is determined visually from the high-speed videos. Figure S9 shows snapshots of the developed kinks, taken 2/3 of the way between the kink formation and the final pinch-off.

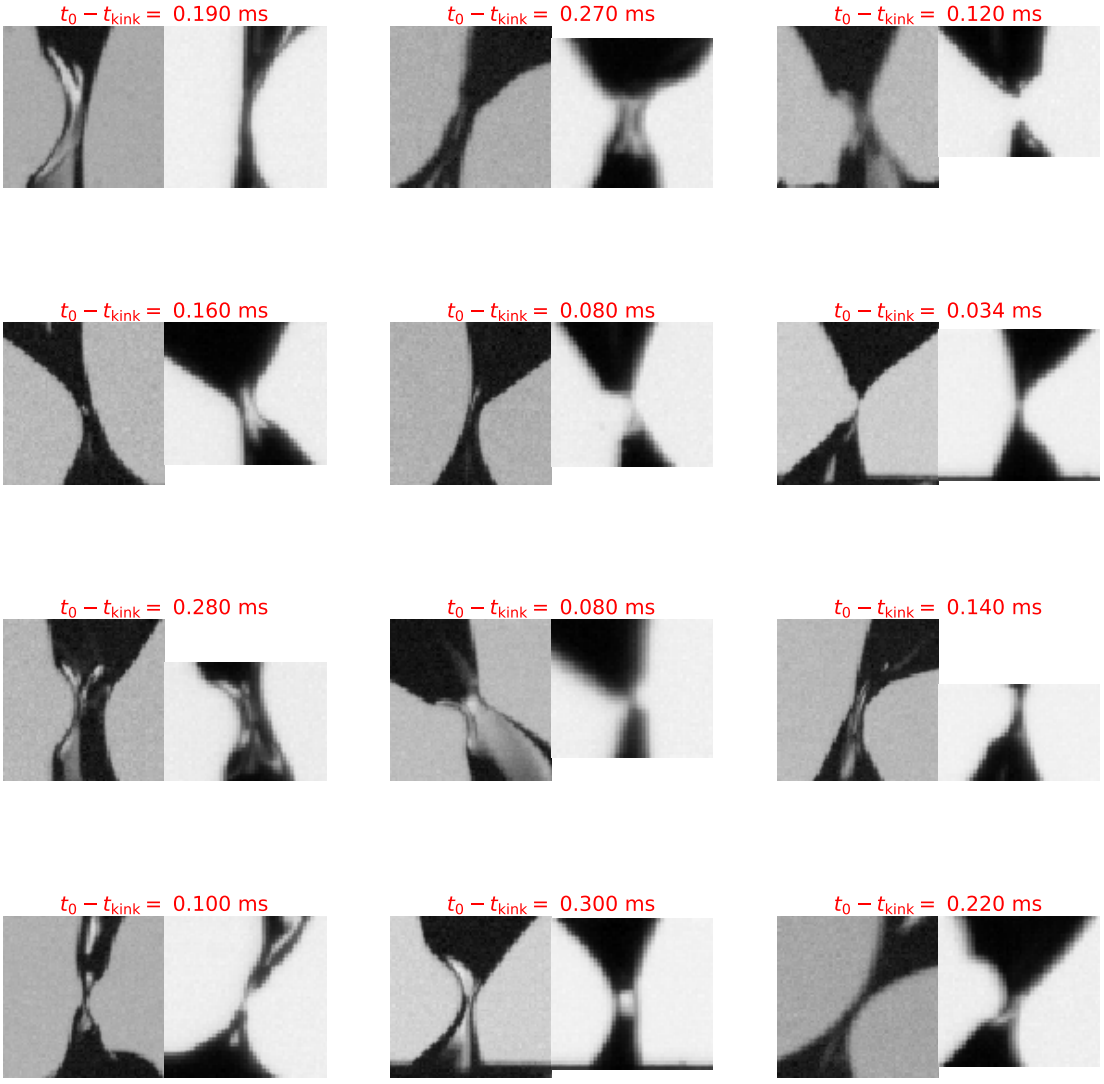

Fig. S9. Snapshots of the neck interface for a sample of 12 cases in which the kink, characterized by an abrupt change in curvature of the neck interface, was observed. The visually-determined time of kink appearance $t = t_0 - t_{\rm kink}$ is shown above each set of images. For each case, the view near the neck region in the $x - z$ and $y - z$ planes are shown at $t \approx t_0 - t_{\rm kink}/3$ to give a structure of the developed kink. Each image is $1.5\,{\rm mm}$ wide.

3. Numerical simulations

For the numerical simulations, the Basilisk solver (7–9) is used in three dimensions to solve the nonlinear incompressible Navier-Stokes equations in two phases with surface tension, where a momentum-conserving volume-of-fluid advection scheme is used to reconstruct the liquid-gas interface. Octree-type adaptive mesh refinement is used in order to minimize the computational requirements, and the refinement criteria are chosen so that maximum resolution is achieved on the bubble neck only in the final stages of pinch-off. In the simulations, the full bubble shapes are initialized in a quiescent medium, and the ratio between the liquid density ρ_1 and gas density ρ_2 is $\rho_1/\rho_2 = 850$; the corresponding viscosity ratio is $\mu_1/\mu_2 = 5.12$. The simulations do not include gravity and hence neglect buoyant effects. We consider three simulations, an axi-symmetric

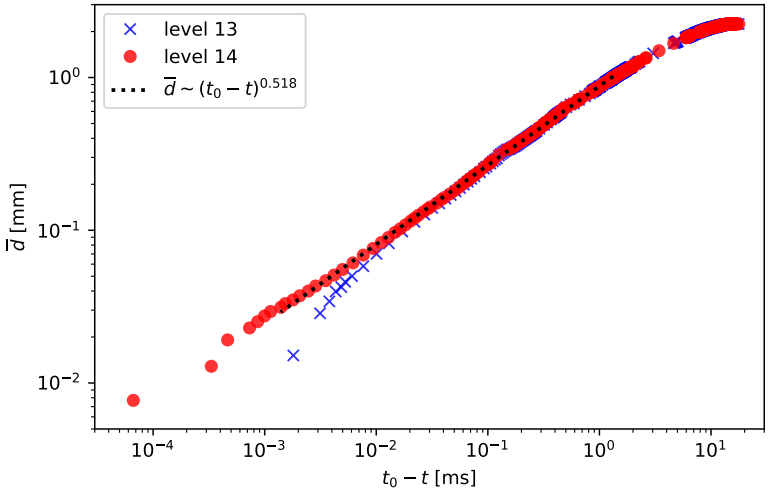

Fig. S10. Numerical convergence for the 3D axisymmetric case. The two highest resolution cases are shown and exhibit both the self-similar pinch-off process, the higher resolution achieving a thinner neck as expected.

configuration, used to validate the numerical approach, and axi-symmetric configuration with small elliptical perturbation on the neck, to reproduce the neck oscillation observed experimentally, and finally an asymmetric configuration to reproduce the escape from self-similarity behavior.

We define the cylindrical interface profile of the axisymmetric bubble,

$$\hat{r}(\theta) = -\sin(\theta)(1 + bP_2(\cos\theta)), \quad \hat{z}(\theta) = \cos(\theta)(1 + aP_2(\cos\theta)), \qquad [13]$$

where $P_2(x)$ is the second-order Legendre polynomial, $\theta \in [0, \pi)$ is the polar angle, and $a = 0.5, b = 1.8$ produces an axisymmetric initial bubble with a neck prior to pinch-off. This configuration is inspired by earlier work from Lister (10), showing that such axi-symmetric initial shape lead to self-similar collapse of the bubble, independently of the particular values of the coefficient a and b which set the dumbbell shape.

The typical initial neck radius r_0 obtained with this initialization is related to the maximum bubble dimension D_0 by $r_0/D_0 = 1/30$. The domain length is set to $L_0 = 1.2D_0$. The liquid phase sets the mass scale through its density ρ_1, and a timescale through surface tension γ such that $\tilde{t} = \sqrt{\rho/(\gamma r_0^3)}$. The kinematic viscosity is set to $\nu_1 = 3.2 \times 10^{-2} r_0^2/\tilde{t}$, corresponding to a Laplace number of $\mathrm{La} = 2r_0\gamma/(\rho_1\nu_1^2) = 2 \times 10^5$, which is similar to that of water-air interfaces at millimetre length scales.

The neck sizes are extracted from the simulations by exporting the bubble interface as an .stl file and taking a slice through the pinch-off plane, yielding a set of line segments defining the intersection of the bubble interface and this plane. d_x is the maximum of the x values of the endpoints of these segments minus the minimum of the x values, and d_y is calculated in the same way.

Grid convergence is achieved with respect to the neck thinning rate at times leading up to pinch-off, according to tests performed on the three-dimensional axisymmetric cases. Resolutions of $\Delta x = L_0/2^l$ with $l = 13, 14$ are tested for the three-dimensional case. The mesh adaptive refinement criterion is set so that the neck diameter is resolved with $6 - 10$ points throughout the pinch-off process. Thus the effective resolutions $l = 13, 14$ allow for the final neck to represented at approximately $250,450$ times thinner than the initial neck, with the highest resolution reached close to pinch-off. Figure S10 shows the neck thickness profiles for these cases, with the pinch-off time calculated as the time at which the neck diameter reaches $3\Delta x$. For each case, the two curves are indistinguishable for most of the pinch-off process, and only diverge slightly from each other at around 10^{-5} to 10^{-4} time units before pinch-off when they reach their respective maximum resolutions. The exponents on the curves match the expected theoretical and experimental result with $\alpha = 0.5$. The axisymmetric case is shown in Figure S11(a)-(d). These results are in excellent agreement with the theoretical prediction and earlier numerical work (10–12).

Now, we introduce corrections to the initial shape. Using Cartesian coordinates, non-axisymmetric corrections can be introduced,

$$x(\phi, \theta) = \hat{r}(\theta)\cos\phi(1 + e) + \frac{T_0 z_0^2}{z(\phi, \theta)^2 + z_0^2}, \quad y(\phi, \theta) = \hat{r}(\theta)\sin\phi(1 - e), \quad z(\theta) = \hat{z}(\theta). \qquad [14]$$

where $\phi \in [0, 2\pi)$ is the azimuthal angle. Recall, the axisymmetric bubble corresponds to $T_0 = z_0 = e = 0$; a bubble with a slight elliptical eccentricity sets $e = 0.1$; and the non-axisymmetric case uses the tilt parameter $T_0 = 0.7$ and $z_0 = 0.5, e = 0$.

The axisymmetric case is shown in Figure S11(a)-(d), the elliptic in (e)-(h), and the tilted non-axisymmetric case in (i)-(l). The times of each snapshot vary but show in sequence the initial, early, late, and pinch-off stages for each case. In each case,

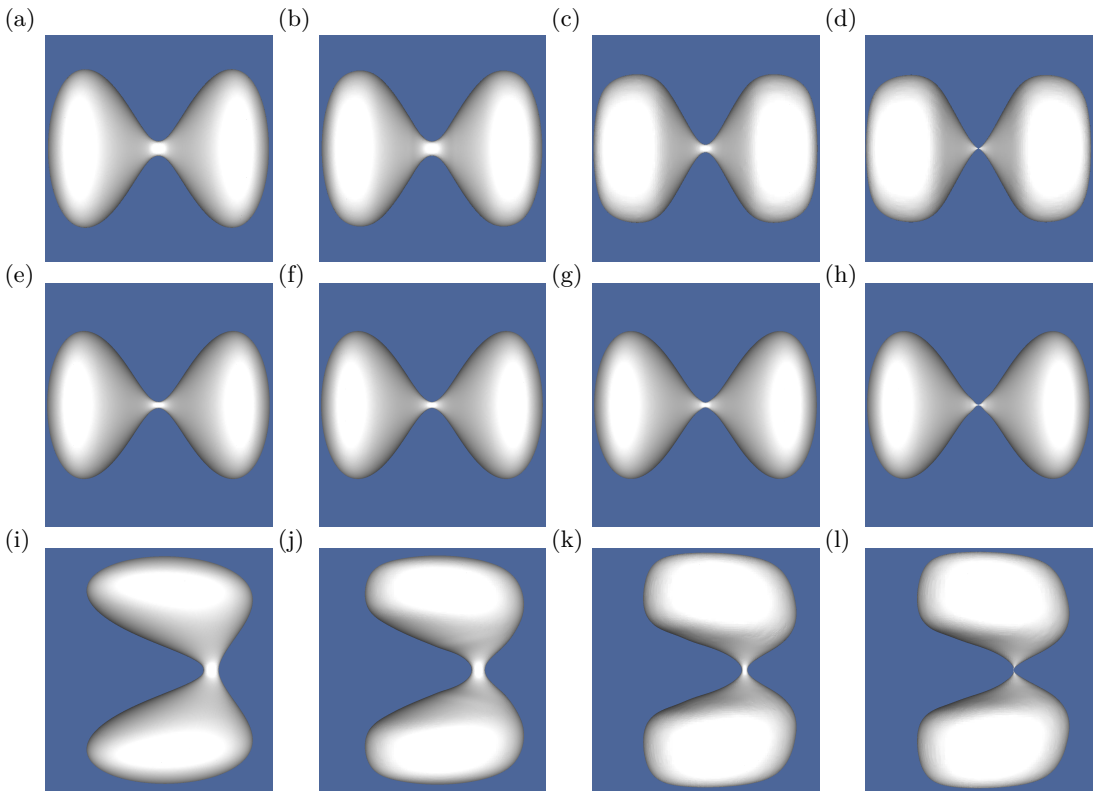

Fig. S11. Snapshots of pinch-off process for various bubble geometries and initial conditions: (a)-(d) axisymmetric (two-dimensional), (e)-(h) axisymmetric (three-dimensional), (i)-(l) elliptical, (m)-(p) tilted non-axisymmetric.

the entire bubble evolves during the simulation; while the neck thins, the lobes of the bubble become more bulbous. In the case of the non-axisymmetric case, the asymmetry in the curvature is apparent and influences strongly the pinch-off process, as described in the main paper.

For the elliptic case, the neck sizes d_x and d_y are shown in the left of Figure S12 (in blue and green) along with the average neck size (in red) which follows a power-law with $\overline{d} = (t_0 - t)^{0.53}$ for much of the collapse. The oscillation signal $(d_x - d_y)/2$ is shown on the right, along with a fit to the model described by eq. 1 in the main paper. The oscillatory behavior observed experimentally is reproduced qualitatively, with good agreement between the numerical data and theoretical model.

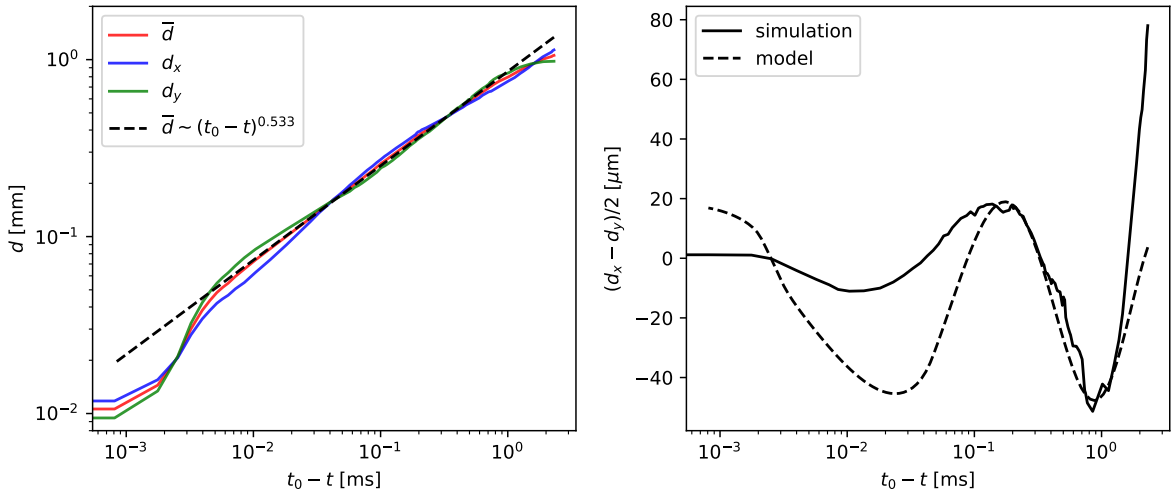

Fig. S12. The simulated neck collapse when starting with an elliptical shape.

In addition to the base non-axisymmetric case with $T_0 = 0.7$, we include cases with $T_0 = 0.7, 0.8, 0.9, 1$ in order to determine the effect of the degree of asymmetry in the initial condition on the kink formation diameter $\bar{d}_k$. For the case $T_0 = 1$, we set $b = 1.85$. For these cases the maximum resolution is $l = 12$ but the refinement criterion is tuned to allow for an effective resolution of $8 - 14$ cells on the neck or greater throughout the pinch-off process to obtain better resolution of the neck at the moment of kink formation. We verify convergence separately for these cases with an additional simulation for $T_0 = 0.8$ at $l = 14$ which was restarted prior to kink formation from an $l = 10$ simulation, in Figure S13, showing close comparison for neck asymmetry (left) and neck growth rate (right) with respect to neck size close to pinch-off.

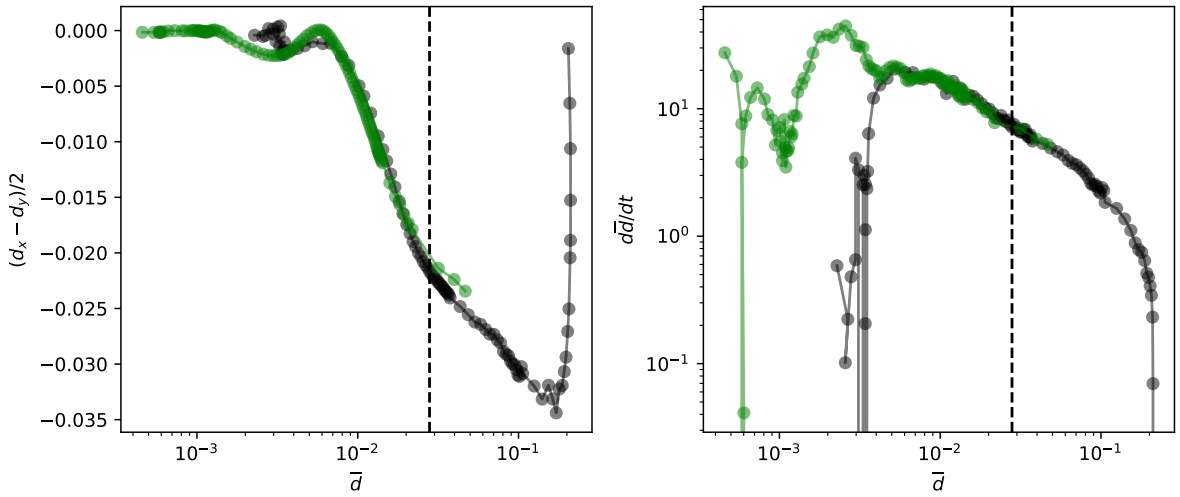

Fig. S13. Numerical convergence for the $T_0 = 0.8$ asymmetric case, comparing a case with $l = 12$ (black) and $l = 14$, which is initialized at a certain point into a $l = 10$ simulation. *Left* shows the neck asymmetry $(d_x - d_y)/2$ as a function of the average neck size $\overline{d}$, both taken in the $z = 0$ plane. *Right* shows the collapse rate $-d\overline{d}/dt$ against the neck size $\overline{d}$. The point of kink formation is denoted by the dashed line.

4. Statistics of kink formation

The parameter space for the experiments is shown in Figure S14, which lists the number of experiments considered at each condition. Since the bubble is pinned to a fixed needle before pinch-off, turbulent motions at scales much larger than the bubble (of typical velocity u'_{rms}) sweeping past the needle induce stresses stretching the bubble that are balanced by surface tension at a scale $l_{\mathrm{stretch}} = \sigma/(\rho u'^2_{\mathrm{rms}})$, which spans from $0.4d_{\mathrm{n}}$ to $5d_{\mathrm{n}}$. This length scale is also set by the turbulence and surface tension, so that there is a strong correlation between $l_{\mathrm{stretch}} \sim \epsilon^{-2/3}$ and the Hinze scale $d_{\mathrm{H}} \sim \epsilon^{-2/5}$ as shown on the left in Figure S14. We expect the role of the large-scale motions characterized by l_{stretch} to be primarily to deform the bubble as a whole, while turbulent motions at the neck scale are responsible for the neck-scale deformations. The parameter space is also shown in terms of the ratio between the needle size and the Taylor microscale of the turbulence λ in the right of Figure S14.

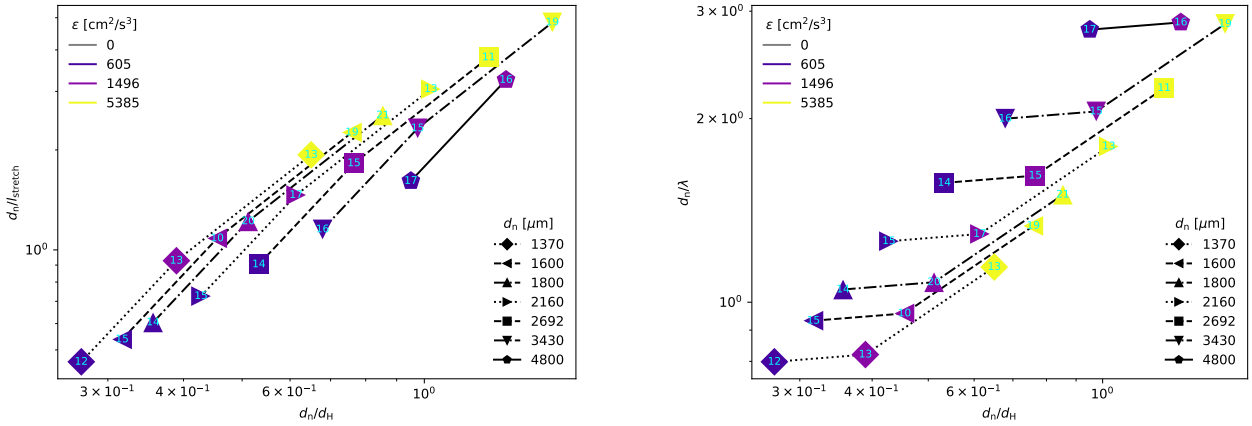

Fig. S14. *Left*, the parameter space of all the experiments run in terms of the needle size d_{n} divided by $l_{\mathrm{stretch}} = \sigma/(\rho u'^2_{\mathrm{rms}})$ and $d_{\mathrm{H}} = (\sigma/\rho)^{3/5}\epsilon^{-2/5}/2$. The number of experiments considered at each condition is shown in cyan. In addition to the data shown on the plot, at least three runs were conducted without turbulence for each needle size. *Right*, the parameter space in terms of the $d_{\mathrm{n}}/d_{\mathrm{H}}$ and d_{n}/λ, where λ is the Taylor microscale of the turbulence.

We show in Figure S15 the $d_{\mathrm{n}}/d_{\mathrm{H}}$ dependence of the power-law exponents α obtained by fitting a power-law collapse to the mean neck diameter. This contains the same data as is aggregated into a single distribution in Figure 4 in the main paper. The distributions are all centered near $\alpha = 1/2$, with the spread of exponent values increasing as the turbulence parameter is increased.

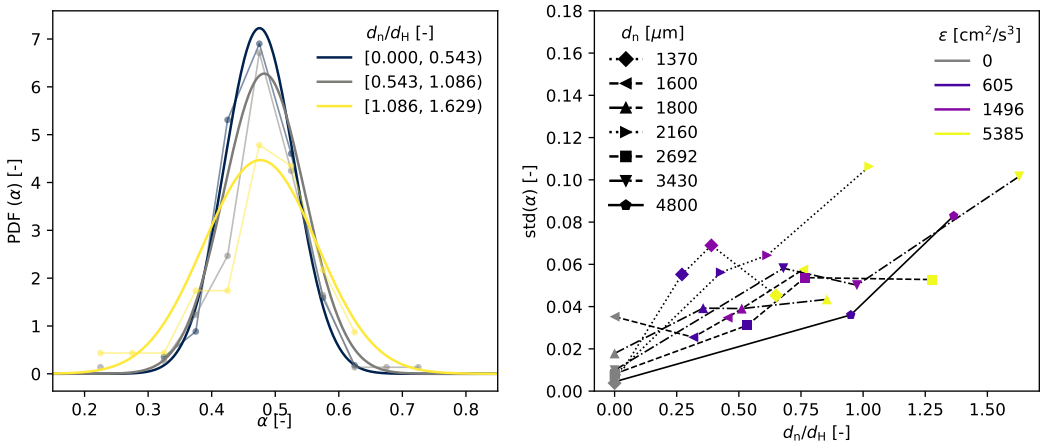

Fig. S15. The effect of $d_{\mathrm{n}}/d_{\mathrm{H}}$ on the measured power-law exponent. The distribution of α values fit to the data, binned by $d_{\mathrm{n}}/d_{\mathrm{H}}$, is shown on the left. The standard deviation of α for each experimental condition is shown on the right.

The maximum neck asymmetries reported for the experiments in the main paper are measured in the range when the neck size is smaller than $d_{\mathrm{n}}/3$ and, for the cases that kink, greater than $\overline{d}_{\mathrm{k}}$. This maximum asymmetry tends to increase with the needle size and the turbulence dissipation rate, as is evidenced in Figure S16, which shows the distributions of the maximum asymmetries measured at each experimental condition.

The larger this asymmetry is, the more likely a kink is to form. Figure S17 shows the likelihood of a kink forming given the measured maximum asymmetry for each needle. This plot confirms that the correlation between neck asymmetry and

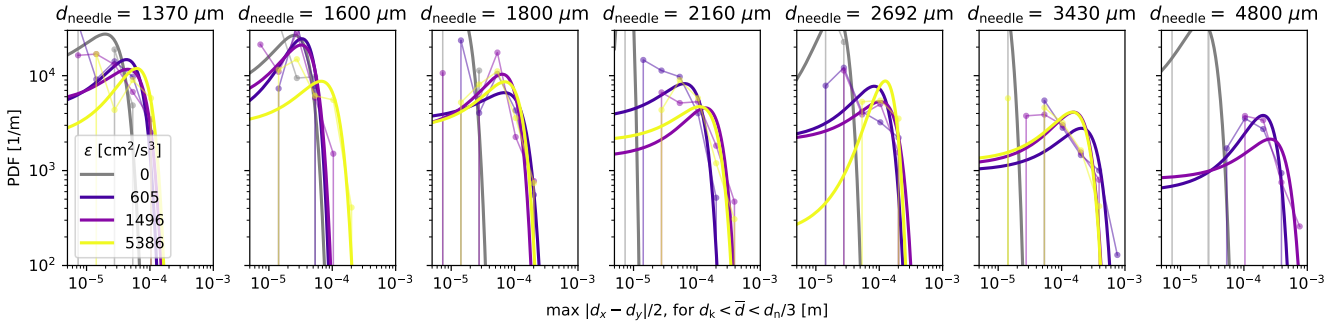

Fig. S16. The distribution of maximum neck asymmetries $|d_x - d_y|/2$ observed for each combination of d_n and ϵ. This metric of the neck deformation tends to increase as either parameter is increased. The raw distributions are shown with the symbols and faint lines; Gaussian fits are shown in the thicker lines.

kink formation persists even after the needle size is controlled for. As additional evidence, we consider that the normalized covariance between $\max|d_x - d_y|/2$ and $\overline{d}_k$, plotted in Figure 3 in the main paper, is 0.748. We then calculate the normalized covariance between the two parameters within each experimental condition defined by ϵ and d_n, and find that the mean of all these normalized covariances is 0.523, with the standard deviation being 0.208. Thus, after controlling for the two independent variables in our experiment, there is a positive correlation between the neck asymmetry and kink formation size.

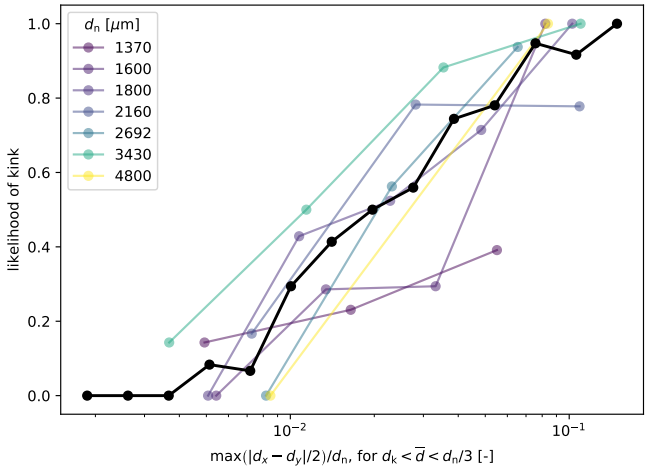

Fig. S17. The likelihood of a resolvable kink occurring given the needle size and the maximum asymmetry observed. Data is shown for individual needles as the colored lines, and for all the data as the black line.

In the paper, we characterize the point of kink formation by the size of the neck when the first indication of the kink is observed, $\overline{d}_k$. Another possible choice would have been to report $t_0 - t_k$, the time of the kink formation before pinch-off. However, this value is set by both the point into the collapse at which the kink forms *and* the speed of the kinked collapse, making $\overline{d}_k$ a more straightforward metric. Figure S18 shows the high correlation between $\overline{d}_k$ and $t_0 - t_k$. The data can be described by a power law fit, $(t_0 - t_k) \propto \overline{d}_k^{1.38}$. The data is in close agreement with the capillary time at the kink scale, $\tau_{cap,k} = \sqrt{\rho(\overline{d}_k/2)^3/(2\pi\sigma)}$, which is shown as the red dashed line.

The distribution of kink sizes and kink times is shown for various bins of d_n/d_H in Figure S19. As it is increased, the kinks tend to appear earlier on and are larger.

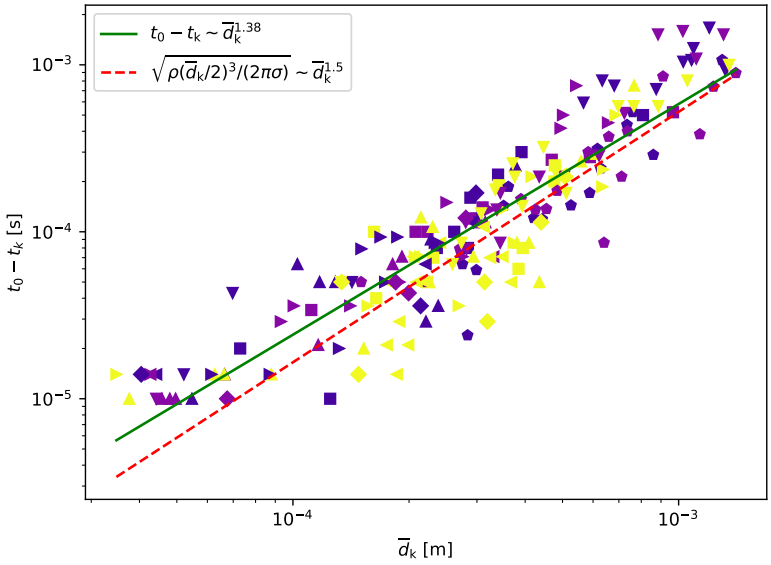

Fig. S18. The kink time against the kink size. The colors and markers correspond to ϵ and d_{n}, respectively, as indicated in Figure S14. The fit line shown in green is $(t_0 - t_{\mathrm{k}}) \sim \overline{d}_{\mathrm{k}}^{1.38}$, which is close to the capillary time given the kink size, shown as the dashed red line.

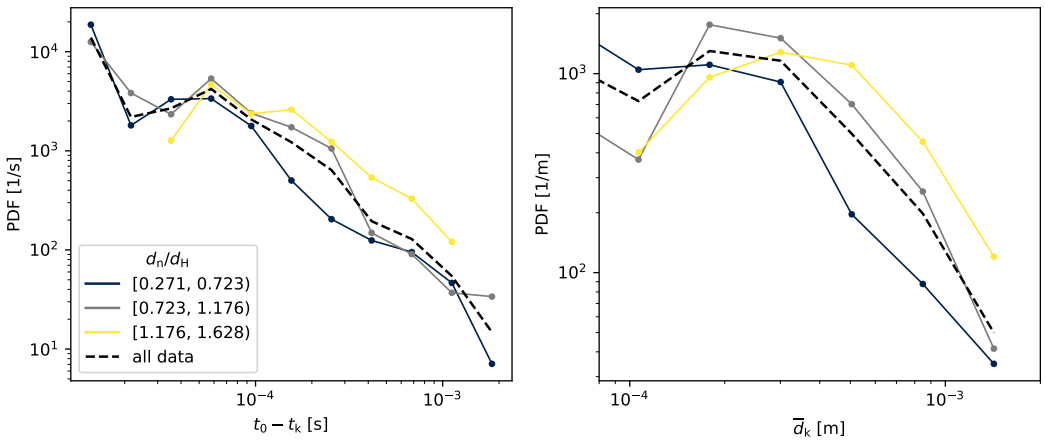

Fig. S19. Distributions of the kink appearance time (left) and the kink appearance size (right) for different values of $d_\mathrm{n}/d_\mathrm{H}$ (color-coded) and ensemble averaged (black dashed lines). The kink size increases with increasing $d_\mathrm{n}/d_\mathrm{H}$.

References

1. EA Variano, EA Cowen, A random-jet-stirred turbulence tank. *J. Fluid Mech.* **604**, 1–32 (2008).
2. W Hwang, JK Eaton, Creating homogeneous and isotropic turbulence without a mean flow. *Exp. Fluids* **36**, 444–454 (2004).
3. W Thielicke, EJ Stamhuis, PIVlab - Towards User-friendly, Affordable and Accurate Digital Particle Image Velocimetry in MATLAB. *J. Open Res. Softw.* **2** (2014).
4. SB Pope, *Turbulent Flows.* (Cambridge University Press), (2000).
5. NC Keim, P Møller, WW Zhang, SR Nagel, Breakup of air bubbles in water: Memory and breakdown of cylindrical symmetry. *Phys. Rev. Lett.* **97**, 1–4 (2006).
6. LE Schmidt, NC Keim, WW Zhang, SR Nagel, Memory-encoding vibrations in a disconnecting airbubble. *Nat. Phys.* **5**, 343–346 (2009).
7. S Popinet, Gerris : a tree-based adaptive solver for the incompressible Euler equations in complex geometries. *J. Comput. Phys.* **190**, 572–600 (2003).
8. S Popinet, An accurate adaptive solver for surface-tension-driven interfacial flow. *J. Comp. Phys.* **228 (16)**, 1–47 (2009).
9. S Popinet, Numerical Models of Surface Tension. *Annu. Rev. Fluid Mech.* **50**, 49–75 (2017).
10. JR Lister, HA Stone, Capillary breakup of a viscous thread surrounded by another viscous fluid. *Phys. Fluids* **10**, 2758–2764 (1998).
11. J Eggers, MA Fontelos, D Leppinen, JH Snoeijer, Theory of the collapsing axisymmetric cavity. *Phys. Rev. Lett.* **98**, 1–4 (2007).
12. M Garzon, LJ Gray, JA Sethian, Simulation of the droplet-to-bubble transition in a two-fluid system. *Phys. Rev. E - Stat. Nonlinear, Soft Matter Phys.* **83**, 1–14 (2011).